Preferential Dynamic Grain Growth Mechanism Enabling the Control of Microstructure and Texture by High Temperature Deformation: Experimental Evidence and Applicability

Hiroshi Fukutomi[1,2,*], Kazuto Okayasu[3], Yusuke Onuki[4], Makoto Hasegawa[2,3], Equo Kobayashi[2,5], Bohumir Strnadel[2] and Osamu Umezawa[2,3]

[1]*Kanagawa Study Center, The Open University of Japan, Yokohama 232-8510, Japan*
[2]*Centre for Advanced and Innovative Technologies, Technical University of Ostrava,*
17. listopadu 2172/15, 708 00 Ostrava-Poruba, Czech Republic
[3]*Division of Systems Research, Faculty of Engineering, Yokohama National University, Yokohama 240-8501, Japan*
[4]*Frontier Research Center for Applied Atomic Sciences, Ibaraki University, Tokai, Ibaraki 319-1106, Japan*
[5]*Department of Materials Science and Engineering, School of Materials and Chemical Technology, Tokyo Institute of Technology,*
Tokyo 152-8552, Japan

The relationship between the mechanism of high temperature deformation and the evolution behavior of microstructure and the texture during deformation, which has been found in various solid solution alloys, is clarified. It is shown that the preferential dynamic grain growth (PDGG) mechanism proposed by the authors can explain the behavior of microstructure change as well as texture change of all studied alloys without contradiction. The essential aspect of the PDGG mechanism is the preferential growth of crystal grains with the orientation stable for deformation and with low Taylor factor in the given deformation mode. It is concluded that the Taylor factor corresponds to dislocation density and stored energy during the high temperature deformation of solid solution alloys when viscous glide of dislocations is the rate controlling process. The possibility of the occurrence of the PDGG mechanism in materials other than solid solution alloys is also discussed.
[doi:10.2320/matertrans.MT-M2021162]

1. Introduction

Various phenomena — such as solute atmosphere dragging of dislocations, grain boundary sliding, and dynamic recrystallization — appear at high temperature deformation depending on temperature, grain size, strain rate and the amount of strain. These phenomena generate microstructures, dislocation structures, and textures that are different from those formed by room temperature deformation. Okayasu and Fukutomi found a change in texture accompanying microstructure change in a uniaxial compression of Al–3.0 mass%Mg solid solution alloy.[1] The uniaxial compression deformation led to the formation of ⟨011⟩ (compression axis) texture at the beginning of the deformation, followed by a transition to ⟨001⟩ (compression axis) texture in the later stage of the deformation. The formation of ⟨001⟩ fiber texture by high temperature uniaxial compression has been reported for Al–2 mass%Mg by Chen and Kocks.[2] They concluded that the formation of ⟨001⟩ texture was attributable to dynamic recrystallization by enhanced nucleation around TiB₂ particles.

The transition process of the texture from ⟨011⟩ to ⟨001⟩ has been studied in detail by Okayasu, Takekoshi and Fukutomi;[3] they concluded that the texture change from ⟨011⟩ to ⟨001⟩ should be attributed to grain boundary migration enlarging the ⟨001⟩ oriented regions. It has been pointed out that dislocation structure caused by the solute atmosphere and orientation stability contributed to the preferential growth of ⟨001⟩ oriented grains. Based on a series of investigations conducted on Al–3.0 mass%Mg, Al–

5.0 mass%Mg and Al–10 mass%Mg,[4,5] a hypothesis on this phenomenon, namely the simultaneous change of microstructure and texture during high temperature deformation, was proposed and experimental examination was conducted on solid solution alloys with FCC and BCC structures. It was found that the hypothesis was applicable irrespective of crystal structure.

The hypothesis[6,7] consists of two assumptions: (1) the texture transition accompanying change of microstructure results from the preferential growth of grains with specific orientation driven by the stored energy difference between neighboring grains originating from dislocations, and (2) growing grains are stable for the deformation in the given deformation mode. In order to find the low stored energy grains, it was assumed that the Taylor factor corresponded to stored energy. It was thus expected that texture change occurs when low Taylor factor orientation is stable for the deformation and different from the usual deformation texture. The experimental results on Fe–3.0 mass%Si with BCC structure was in consistent with the hypothesis, and the hypothesis was named the preferential dynamic grain growth (PDGG) mechanism.[6,7]

Thus the PDGG mechanism was developed on the basis of experimental results. However, the mechanism is not yet understood enough in relation to the deformation mechanism.

In this paper, previously reported experimental results as well as recent outcomes are considered and the generality of the PDGG mechanism is explored. Then, the relationship between the mechanism of high temperature deformation and PDGG mechanism is discussed. Finally, the deformation conditions in which PDGG mechanism operate is discussed.

*Corresponding author, E-mail: fukutomi-hiroshi-pk@ynu.ac.jp

2. Experiment

In this paper, the results of uniaxial compression deformation and plane strain compression deformation in FCC solid solution alloys (Al–3.0 mass%Mg, Al–5.0 mass%Mg, Al–10.0 mass%Mg, and Fe–Mn–Si–Cr[8]) and a BCC solid solution alloy (Fe–3.0 mass%Si[6]) are given. For comparison, experiments were conducted for commercial pure aluminum AA1050[7] and Al–3.0 mass%Mg–0.2Sc, which consists of α phase with Al_3Sc precipitates.

Screw-driven type testing machines (DCS-2000 and AG-X 50 kN, Shimadzu Co., Ltd., Kyoto, Japan) equipped with an infrared ray furnace were used for the deformation test. Cylindrical specimens for uniaxial compression and rectangular specimens for plane strain compression were prepared using a spark erosion machine. The aspect ratio of the cylindrical specimens was 1.5 for all specimen sizes. The diameter of the specimens for uniaxial compression was 12 mm in most cases. All the specimens were homogenized in the single phase state before deformation. Details of the experiments are available elsewhere.[5–8] Figure 1 shows the configuration of the specimens and tools for plane strain compression deformation. After deformation up to the target strain, the specimens and the tools were removed from the furnace and quenched in water.

Texture measurements were conducted on the mid-plane sections of the specimens by the Schulz reflection method using Cu Kα radiation. The {111}, {001} and {011} pole figures were measured, and the orientation distribution function (ODF) was calculated by the Dahms-Bunge method[9] or the ADC method.[10] Textures were investigated on the basis of pole figures and inverse pole figures calculated from the ODF and the φ_2 section of the ODF. Electron backscatter diffraction (EBSD) measurements were conducted to evaluate the positional distribution of the texture components.
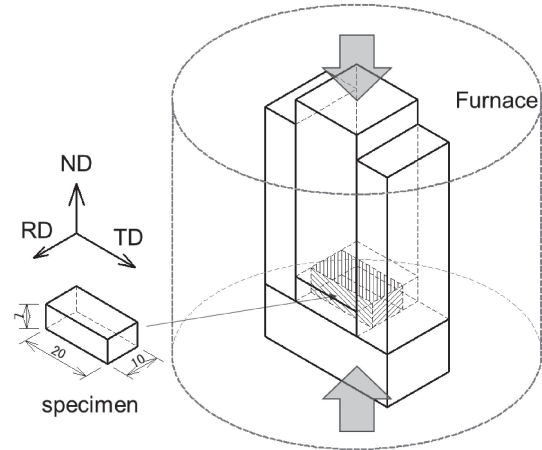

Fig. 1   Tools and a specimen for the high temperature plane strain compression.

3. Results

3.1 Characteristics of the phenomenon elucidated by uniaxial compression experiments on Al–3.0 mass%Mg solid solution

3.1.1 Effects of strain and deformation temperature on texture formation

Figure 2 shows the effect of strain on the texture development of Al–3.0 mass%Mg during the uniaxial compression deformation in the α single phase state.[11] The tests were conducted at 723 K with a strain rate of $5.0 \times 10^{-4} \, s^{-1}$. The development of a fiber texture was confirmed by pole figures. These inverse pole figures depict the distribution of the compression axis density. The mean axis density was used as a unit to draw the contours.

At the early stage of deformation, such as -0.6 in true strain, the area of high axis density appears at $\langle 001 \rangle$ as well as at $\langle 011 \rangle$. The maximum axis density exists at $\langle 011 \rangle$, i.e. the main component of the fiber texture is $\langle 011 \rangle$, which usually appears in the uniaxial compression of metals and
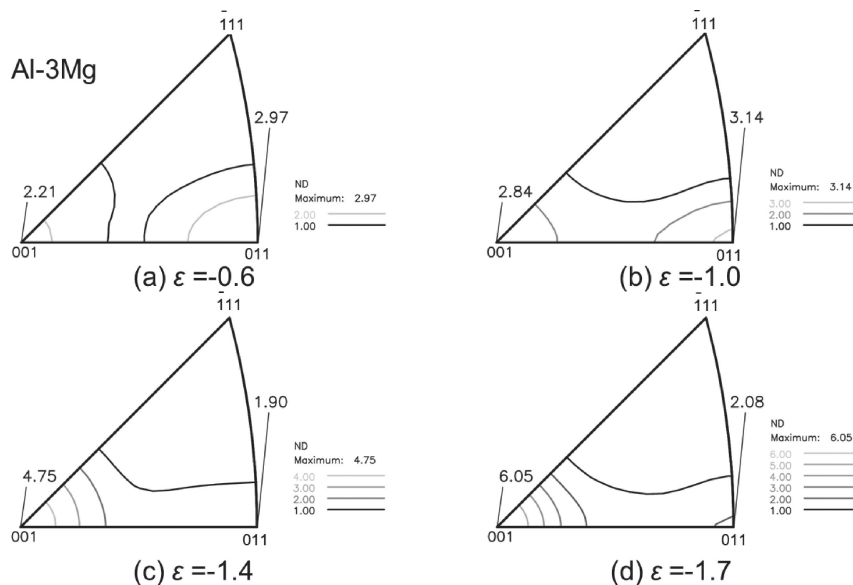

Fig. 2   Inverse pole figures showing the density distribution of the compression axis after deformation at 723 K with a strain rate of $5.0 \times 10^{-4} \, s^{-1}$ up to various amounts of strain. The mean axis density was used for drawing the contours.
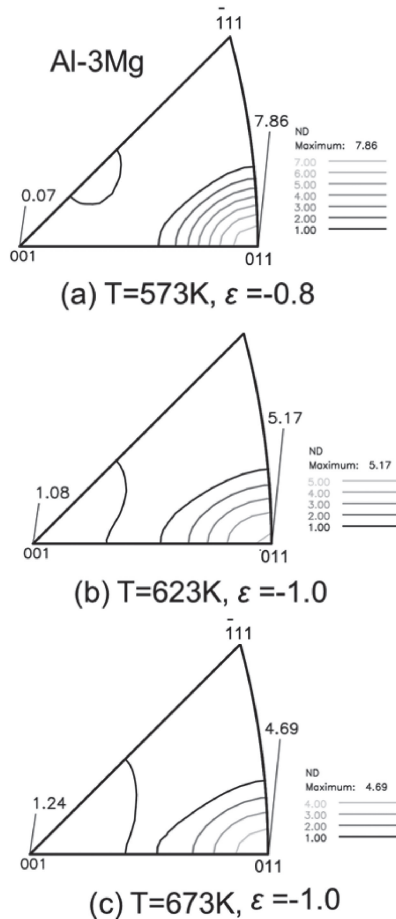
(a) T=573K, ε =-0.8

(b) T=623K, ε =-1.0

(c) T=673K, ε =-1.0

Fig. 3   Effect of deformation temperature on the density distribution of the compression axis.

Fig. 4   Cross section of Al–3.0 mass%Mg and Al–10 mass%Mg deformed at 723 K with a strain rate of $5.0 \times 10^{-4}\,\mathrm{s}^{-1}$ up to approximately -1 in true strain. The colors express the orientation of the compression axis.

discontinuously, such as twinning, nucleation of new grains, and migration of existing grain boundaries.

In order to identify the mechanism of the orientation change during the deformation, EBSD measurements were conducted on the cross section of the deformed specimen.

Figure 4 shows the microstructure of Al–3.0 mass%Mg and Al–10 mass%Mg deformed at 723 K with a strain rate of $5.0 \times 10^{-4}\,\mathrm{s}^{-1}$ up to approximately -1 in true strain. The arrow indicates the compression direction. The colors correspond to the orientation of the compression axis given in the standard stereographic triangle. Whereas the crystal grains of Al–3.0 mass%Mg become horizontally-elongated shape, the grains of Al–10 mass%Mg appear to be equiaxed, and their grain boundaries are uneven. With respect to orientations, the grains in the Al–3.0 mass%Mg are a mixture of ⟨001⟩ and ⟨011⟩ oriented grains, while ⟨001⟩ oriented grains make up the majority of grains in Al–10 mass%Mg. These characteristics of the microstructure suggest that grain boundary migration drives the development of the ⟨001⟩ texture, and that the migration is enhanced by an increase in solute concentration. In order to confirm this consideration, Al–3.0 mass%Mg with Al₃Sc precipitates was prepared by heat treating Al–3.0 mass%Mg–0.2 mass%Sc alloy, and the effect of high temperature deformation on the development of microstructure and texture was studied.

Figure 5 shows a cross section of the Al–3.0 mass%Mg with Al₃Sc precipitates after the same deformation as that of Al–3.0 mass%Mg and Al–10 mass%Mg alloys given in Fig. 4. The crystal grains are a mixture of ⟨001⟩ and ⟨011⟩ oriented grains, similar to the grains in the Al–3.0 mass%Mg. It is seen that the frequency of ⟨011⟩ grains in Al–3.0 mass%Mg–0.2 mass%Sc alloy is higher than that in Al–3.0 mass%Mg alloy shown in Fig. 4.

In order to elucidate the effect of Al₃Sc precipitates on the microstructure change quantitatively, the aspect ratio (i.e., the ratio between the grain size along the vertical direction and that along the horizontal direction) of the crystal grains was evaluated. For comparison, the aspect ratio of a spherical grain after uniaxial compression deformed up to -1.0 in true strain was calculated by assuming constant volume. The results are given in Table 1. The aspect ratio of Al–3.0 mass%Mg is 0.73, which is much larger than the value of

alloys with FCC structure after room temperature deformation. It can be seen that the main component of the texture changes from ⟨011⟩ to ⟨001⟩ with increasing strain. After the deformation up to -1.4 and -1.7 in true strains, the axis density at ⟨011⟩ is lower than that at ⟨001⟩. The axis densities at ⟨001⟩ are 4.75 and 6.05 times the mean axis density for strains of -1.4 and -1.7, respectively. The axis densities at ⟨011⟩ are 1.90 and 2.08 for the same strains. Thus, the main component of the fiber texture changed from ⟨011⟩ to ⟨001⟩ with an increase in strain.

Uniaxial compression deformation was conducted with a strain rate of $5.0 \times 10^{-4}\,\mathrm{s}^{-1}$ up to approximately -1 in true strain at 573 K, 623 K, 673 K, and 723 K. Figure 3 shows the density distribution of the compression axes after the deformation at 573 K, 623 K and 673 K. The result at 723 K has already been presented in Fig. 2(b). It appears that the change of the main component of the texture from ⟨011⟩ to ⟨001⟩ is enhanced by an increase in temperature; deformation temperature also affects the texture development.

3.1.2   Microstructure change causing texture evolution

The axis density distribution given in Fig. 2 and Fig. 3 shows distinct characteristics of orientation change. The axis density contours between ⟨011⟩ and ⟨001⟩ are not continuous. Obviously, this means that the change of the main texture component from ⟨011⟩ to ⟨001⟩ is not caused by the lattice rotation originating from the crystal slip deformation, but rather by mechanisms generating large orientation change
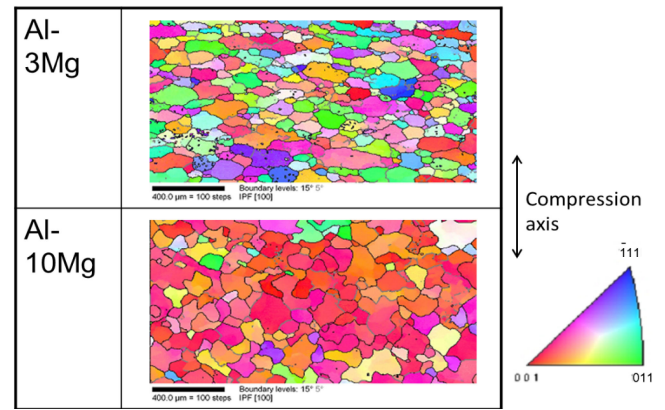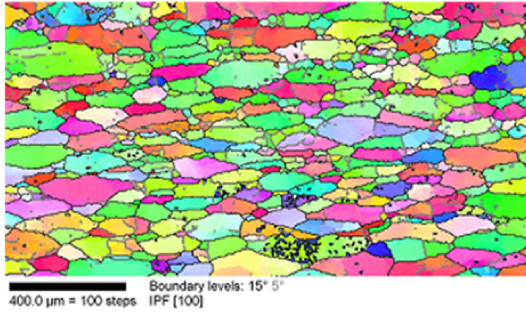
Fig. 5 EBSD observation conducted at the cross section of Al–3.0 mass%Mg–0.2 mass%Sc alloy after uniaxial compression at 723 K with a strain rate of $5.0 \times 10^{-4}\,\mathrm{s^{-1}}$ up to approximately -1 in true strain. The colors express the orientations of the compression axis same as Fig. 4.

Table 1 Aspect ratios of crystal grains of Al–3.0 mass%Mg and Al–3.0 mass%Mg with Al$_3$Sc precipitates after uniaxial compression up to approximately -1 in true strain. The deformation was conducted at 723 K with a strain rate of $5.0 \times 10^{-4}\,\mathrm{s^{-1}}$. For comparison, the geometrical calculation for a spherical grain is given.

	Aspect ratio
Calculation	0.22
Al-3.0mass%Mg	0.73
Al-3.0mass%Mg-0.2mass%Sc	0.33

0.22 derived by the calculation. On the other hand, the ratio for Al–3.0 mass%Mg with Al$_3$Sc precipitates is close to the value derived by the calculation. This means that grain boundary migration occurs extensively in Al–3.0 mass%Mg alloy, while the migration is limited in Al–3.0 mass%Mg with Al$_3$Sc precipitates. Thus, it is concluded that the change of the main component of the fiber texture from $\langle 011 \rangle$ to $\langle 001 \rangle$ can be attributed to the extensive grain boundary migration which expands the $\langle 001 \rangle$ oriented regions.

Figure 6 shows the inverse pole figures of Al–3.0 mass%Mg with Al$_3$Sc precipitates after the deformation at 723 K up to -1.0 in true strain. The main component of the texture is $\langle 011 \rangle$ irrespective of strain rates. After the deformation with the strain rate of $5.0 \times 10^{-4}\,\mathrm{s^{-1}}$ up to -1.0 in true strain, the axis density at $\langle 001 \rangle$ is 2.06 as shown in Fig. 6(a). In the case of Al–3.0 mass%Mg shown in Fig. 2(b), the axis density at $\langle 001 \rangle$ is 2.84 which is much higher than that of Al–3.0 mass%Mg with Al$_3$Sc precipitates. This indicates that the development of $\langle 001 \rangle$ is reduced when grain boundary migration is suppressed by the precipitates. Thus, the change of texture from $\langle 011 \rangle$ to $\langle 001 \rangle$ is attributed to grain boundary migration.

3.2 Generality of characteristics found by the uniaxial compression experiments on Al–3.0 mass%Mg alloy

Al–5.0 mass%Mg alloy was subjected to plane strain compression deformation, and the characteristics of its microstructure and texture were compared with those of the Al–3.0 mass%Mg to determine whether the phenomenon occurs generally in solid solution alloys and in deformation modes other than uniaxial compression.

Figure 7(a) shows the $\varphi_2 = 0°$ section of ODF for Al–5.0 mass%Mg after plane strain compression deformation
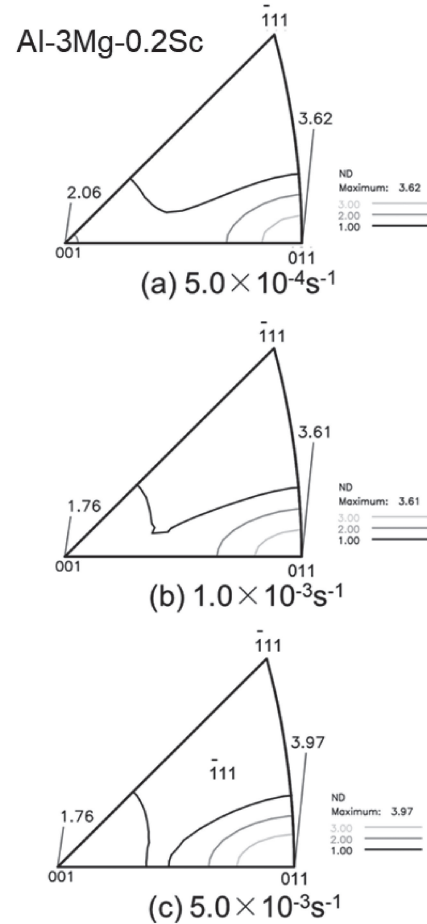

Fig. 6 Inverse pole figures showing the density of the compression axis after uniaxial compression up to -1.0 in true strain at 723 K with three different strain rates.

at 673 K with a strain rate of $5.0 \times 10^{-4}\,\mathrm{s^{-1}}$ up to -1.0 in true strain. The coexistence of texture components known as B ($\{011\}\langle112\rangle$) and Cube orientations ($\{001\}\langle100\rangle$) can be observed. The former is one of the texture components of rolling texture; deformation texture develops in this deformation state.

Figure 7(b) shows the $\varphi_2 = 0°$ section of ODF for Al–5.0 mass%Mg after plane strain compression at 723 K; this is 50 K higher than that of Fig. 7(a) with the same strain rate and strain as in Fig. 7(a). The formation of a sharp cube texture is confirmed.

Thus, it was concluded that the new texture, namely cube texture in this case, developed during high temperature deformation after the development of the usual deformation texture. The same phenomenon occurs as with Al–3.0 mass%Mg.

4. Discussion

4.1 Summary of the experimental results for the uniaxial compression deformation of Al–3.0 mass%Mg described in section 3

The characteristics of the change in microstructure and texture can be summarized as follows.

(1) The change in microstructure and texture begins after the deformation up to a certain amount of strain.

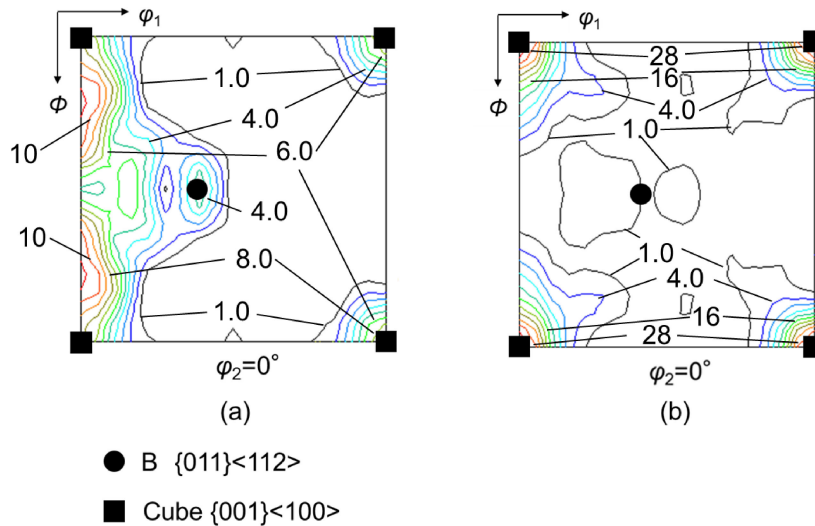Fig. 7   (a) $\varphi_2 = 0°$ section of ODF for Al–5.0 mass%Mg after plane strain compression at 673 K with a strain rate of $5.0 \times 10^{-4}\,\mathrm{s}^{-1}$ up to a true strain of -1.0. (b) $\varphi_2 = 0°$ section of ODF for Al–5.0 mass%Mg after plane strain compression at 723 K; this is 50 K higher than that of (a) with the same strain rate and strain as in (a).

(2) The change occurs depending on deformation temperature and strain.

(3) Expansion of the $\langle 001 \rangle$ region by grain boundary migration is the process that induces the change in microstructure and texture.

(4) An increase in solute concentration enhances the microstructure change from horizontally-elongated shape grains to equiaxed shape grains and the change of texture from $\langle 011 \rangle$ to $\langle 001 \rangle$.

In addition, the following characteristics have been reported in the previous papers.

(5) In pure aluminum, no change in microstructure and texture was seen.[7]

(6) The changes of microstructure and texture occur when the predominant mechanism of high temperature deformation is considered to be the solute atmosphere dragging of dislocations.[5]

(7) Strain rate also affected the occurrence of the change in microstructure and texture.[12]

4.2 The mechanism generating the phenomenon with characteristics summarized in section 4.1

4.2.1 Development of $\langle 011 \rangle$ texture at the initial stage of deformation

Since the specimens are in the annealed state before the tests are conducted, there exists little driving force for the grain boundary migration before the deformation. Therefore, until the stored energy inside the grains reaches levels that are sufficient to cause the grain boundary to migrate, deformation proceeds without any accompanying grain boundary migration. Thus, $\langle 011 \rangle$ texture is initially developed by crystal slip deformation, followed by the development of $\langle 001 \rangle$ texture.

4.2.2 Deformation mechanism driving the preferential growth of $\langle 001 \rangle$ oriented grains; the Taylor factor as an indicator of the stored energy in grains

At high temperatures, two mechanisms are known to be the major rate controlling processes in deformations when dislocation movement is the basic process of deformation:

recovery and solute atmosphere dragging. The former and the latter typically occur in Al[13] and Al–Mg alloys,[14] respectively. As described in point (6) of section 4.1, it was found that changes in microstructure and texture occur when solute atmosphere dragging dominated the dislocation motion.[5]

It is known that the strain rate can be described by the following equations for high temperature deformation, depending on the rate controlling process of dislocation movement:

$$\dot{\varepsilon} = \alpha \dot{\rho}\mathrm{bx} \quad ^{13)} \tag{1}$$

$$\dot{\varepsilon} = \beta \rho_{\mathrm{m}}\mathrm{bv} \quad ^{13)} \tag{2}$$

Equations (1) and (2) hold when the dislocation motion is dominated by recovery and solute atmosphere dragging, respectively. Here, $\dot{\varepsilon}$, α, $\dot{\rho}$, b, and x in eq. (1) are strain rate, geometrical constant, generation rate of mobile dislocations, magnitude of Burgers vector, and mean free path of dislocations, respectively. β, ρ_{m}, and v in eq. (2) are geometrical constant, density of mobile dislocations, and velocity of dislocations, respectively.

It is well known that dislocations form subgrain structures when recovery is the rate controlling process in deformation. Dislocations are waiting to become mobile in this case, because the internal stress is 100% of the applied stress.[13] Equation (1) gives only the generation frequency of the mobile dislocations; this equation provides no information on the density of existent dislocations in the grains.

In the case of eq. (2), the density of dislocations inside the grains can be estimated. One of the characteristics of solute atmosphere dragging is the uniform distribution of dislocations during the deformation due to the effective stress:[14] almost all the dislocations are mobile. When dynamic recovery extensively occurs, subgrain structure develops and the stored energy originating from energy of dislocations is reduced.[13] In contrast, when dislocations are distributed homogeneously, no significant reduction of stored energy occurs, because individual dislocations are isolated. In

this circumstance, the amount of stored energy is considered to be closely related to the dislocation density ρ_m in the crystal grains.

Due to the continuity of the deformation throughout adjacent crystal grains, the summation of shear strains of the activated slip systems—and hence the dislocation density in the individual grains—varies depending on the crystal orientation and deformation mode. In previous papers,[6,7)] it was assumed that the Taylor factor corresponded to the dislocation density in each grain, and indeed the experimental results were consistent with this assumption.[5–8)]

However, no theoretical explanation has been shown on the correlation between the Taylor factor and the stored energy.

The Taylor factor M is defined as the ratio between the summation of shear strains in the activated slip systems and the strain for the given deformation mode. Equation (3) is the definition of the Taylor factor for uniaxial compression:

$$M = \frac{\sum_i |d\gamma_i|}{d\varepsilon} \tag{3}$$

where $d\varepsilon$ and $d\gamma_i$ are the incremental compression strain and the incremental slip on the individual slip systems, respectively. A large value of M indicates large slips in the slip systems; the number of dislocations contributing to the deformation thus increases.[15)]

The value of the Taylor factor is not usually considered to correspond directly with the density of existing dislocations in the grains during deformation, because the strains are merely the results of dislocation gliding; not all the dislocations causing the deformation might be present in the grains during the deformation.

However, in the case of eq. (2), almost all the dislocations are mobile and hence ρ_m in eq. (2) is the density of dislocations in crystal grains. In this case, Taylor factor is related to the dislocation density during the deformation as follows. The numerator of the right side of eq. (3) can be rewritten as eq. (4), using the dislocation densities ρ_{mi} and the incremental mean free paths dx_i of the individual slip systems.

$$\sum_i |d\gamma_i| = \sum_i \rho_{mi}bdx_i \tag{4}$$

Thus, Taylor factor can be given by eq. (5).

$$M = \frac{\sum_i \rho_{mi}bdx_i}{d\varepsilon} \tag{5}$$

The dislocation density ρ_m in eq. (2) and the weighted average of mean free paths $\bar{x}$ can be obtained by eqs. (6) and (7), respectively.

$$\rho_m = \sum_i \rho_{mi} \tag{6}$$

$$d\bar{x} = \frac{\sum_i \rho_{mi}dx_i}{\sum_i \rho_{mi}} \tag{7}$$

The substitution of (6) and (7) into eq. (5) results in eq. (8):

$$Md\varepsilon = \rho_m bd\bar{x}. \tag{8}$$

Equation (9) is the time derivative of eq. (8).

$$M\frac{d\varepsilon}{dt} = M\dot{\varepsilon} = \rho_m b \frac{d\bar{x}}{dt} = \rho_m bv \tag{9}$$

Equation (9) shows that the Taylor factor directly reflects the amount of existing dislocation in the grains.

Thus, it was concluded that grains with low Taylor factor orientation were in the low stored energy state, and expanded by consuming high Taylor factor grains during deformation. As reported by Chin et al.,[16)] the Taylor factor for uniaxial deformation is 2.449 at $\langle 001 \rangle$, which is much smaller than 3.674 at $\langle 011 \rangle$ and $\langle 111 \rangle$, and hence $\langle 001 \rangle$ oriented grains consume $\langle 011 \rangle$ grains.

4.2.3 The development process of $\langle 001 \rangle$ texture

Figure 2 shows that the $\langle 001 \rangle$ component increases monotonously with increasing strain. As is well known, when deformation proceeds by means of crystal slip, crystal lattice rotation occurs toward the stable orientation for the given deformation mode. The stable orientation for uniaxial compression of FCC crystals is $\langle 011 \rangle$; hence, if $\langle 001 \rangle$ is unstable for the deformation, crystal rotation of $\langle 001 \rangle$ oriented grains towards $\langle 011 \rangle$ occurs, and the development of $\langle 001 \rangle$ cannot be observed. However, eight equivalent slip systems can operate for $\langle 001 \rangle$, contributing to the remaining of $\langle 001 \rangle$ oriented grains. That is, $\langle 001 \rangle$ is the quasi stable orientation and therefore $\langle 001 \rangle$ grains become the majority of the grain structure.

4.3 The preferential dynamic grain growth (PDGG) mechanism

Based on the considerations outlined in 4.2.1, 4.2.2 and 4.2.3, the preferential dynamic grain growth mechanism is redefined as follows:

(1) The homogeneous distribution of dislocations due to solute atmosphere dragging enhances the orientation dependence of stored energy during the deformation.

(2) The Taylor factor corresponds to the level of stored energy. Thus the grains with low Taylor factor orientation can grow preferentially.

(3) When stable or quasi stable orientation for the deformation in the given deformation mode is at the same time an orientation with a low Taylor factor, texture is formed by high temperature deformation.

5. Applicability of the PDGG Mechanism

The PDGG mechanism can be applied to alloys irrespective of their crystal structures. As noted in the point (1) of section 4.3, a homogeneous distribution of dislocations is an essential condition for the occurrence of the PDGG mechanism. Thus, if uniform distribution of dislocation is brought about by mechanisms other than solute atmosphere dragging for solid solution alloys, the occurrence of the PDGG mechanism is expected even in pure metals. It is thus appropriate to discuss the applicability of the PDGG mechanism.

One of the characteristics of the PDGG mechanism is that it enables the texture formed by high temperature deformation to be predicted by two steps: (1) Finding the low Taylor factor orientation for the given deformation mode and
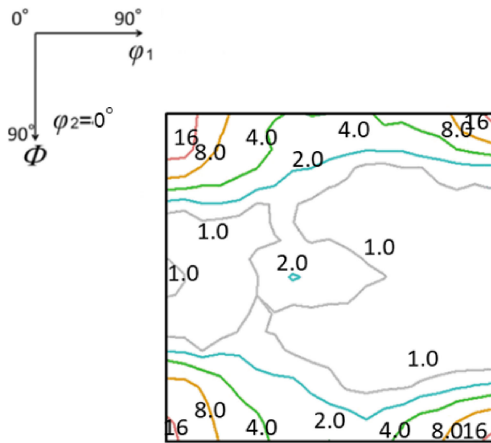
Fig. 8 $\varphi_2 = 0°$ section of ODF for Fe–Cr–Si–Mn alloy after plane strain compression at 1173 K with a strain rate of $5.0 \times 10^{-4}\,\mathrm{s}^{-1}$ up to a true strain of -1.8.

Fig. 9   Orientation dependence of the Taylor factor for the uniaxial deformation of BCC crystals. Slip systems {110}⟨111⟩, {112}⟨111⟩ and {123}⟨111⟩ are taken into account.[17]

Fig. 10   Distribution of compression axis density of Fe–3.0 mass%Si after uniaxial compression deformation at 1173 K with a strain rate of $4.6 \times 10^{-5}\,\mathrm{s}^{-1}$ up to -0.98 in true strain. Mean axis density is used as a unit for drawing the contours.

(2) estimating the stability of low Taylor factor orientation under the given deformation mode.

5.1 Texture prediction by the PDGG mechanism and its experimental verification with FCC alloys other than Al–Mg alloy

A prerequisite for the PDGG mechanism is the uniform distribution of dislocations during the deformation. In the case of alloys, solute atmosphere dragging produces the uniform distribution of dislocations as described above. From this perspective, size effect is an important factor for the occurrence of the PDGG mechanism in solid solution alloys. Two kinds of FCC alloys with large size effects were therefore investigated: Al–Cu alloy[7] and Fe–Cr–Si–Mn alloy.[8] Figure 8 shows the results for Fe–Cr–Si–Mn alloy; the $\varphi_2 = 0°$ section of ODF after plane strain compression deformation is shown. Cube texture is observed, with orientation density higher than 16 times the random level. The Taylor factor calculation for the plane strain compression deformation of FCC materials[7] showed that the Taylor factor for cube orientation is low, consistent with the result in Fig. 8.

5.2 Texture prediction by the PDGG mechanism and its verification by uniaxial and plane strain compression deformation of BCC materials

Figure 9 shows the orientation dependence of the Taylor factor of BCC crystal for uniaxial compression deformation, assuming that {110}⟨111⟩, {110}⟨111⟩ and {123}⟨111⟩ are the active slip systems.[17] The almost minimum Taylor factor 2.12 appears at ⟨001⟩. The deformation texture of BCC crystals for uniaxial compression is well known to comprise fiber textures with ⟨001⟩ and ⟨111⟩ as preferred axes.[18] Because ⟨111⟩ is the maximum Taylor factor orientation, the PDGG mechanism predicts the development of ⟨001⟩ from the viewpoints of the Taylor factor and the stability for deformation. Thus, fiber texture with the main component ⟨001⟩ is expected.

Then, the texture of Fe–3.0 mass%Si alloy with BCC structure was studied experimentally. The uniaxial compression deformation was conducted at 1173 K with a strain rate
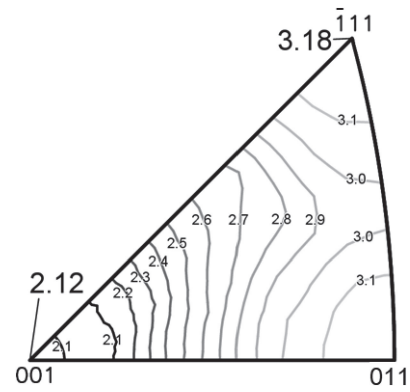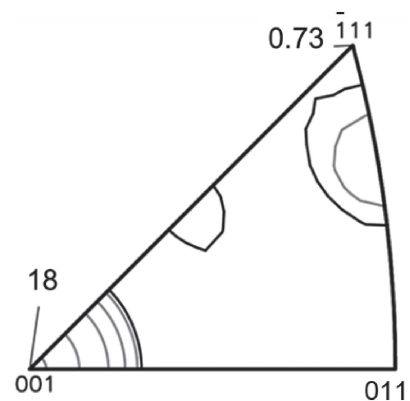
of $4.6 \times 10^{-5}\,\mathrm{s}^{-1}$ to -0.98 in true strain. Figure 10 shows the axis density distribution after the deformation. The maximum axis density exists only at ⟨001⟩, consistent with the prediction.

Figure 11 is the $\varphi_2 = 45°$ section showing the Taylor factor for plane strain compression deformation. In this figure, so-called α fiber and γ fiber, which make up the rolling texture, are depicted by a thick line and a thick broken line with the contours of the Taylor factor. On the basis of this figure, the PDGG mechanism is expected to lead to the development of {001}⟨110⟩, i.e., an orientation satisfying the requirement for both low Taylor factor and stability for the deformation.

Figure 12 shows the result after plane strain compression deformation of Fe–3.0 mass%Si at 1173 K with a strain rate of $5.0 \times 10^{-4}\,\mathrm{s}^{-1}$ up to -1.0 in true strain. The formation of the {001}⟨110⟩ texture is confirmed.

5.3 Deformation conditions for the occurrence of the PDGG mechanism

Figure 13 shows the effects of deformation temperature and strain rate on the axis density at ⟨001⟩ (the axis density of the main component of the fiber texture predicted by the PDGG mechanism, hereafter denoted as P(001)) and at ⟨011⟩ (hereafter denoted as P(011)), as investigated using
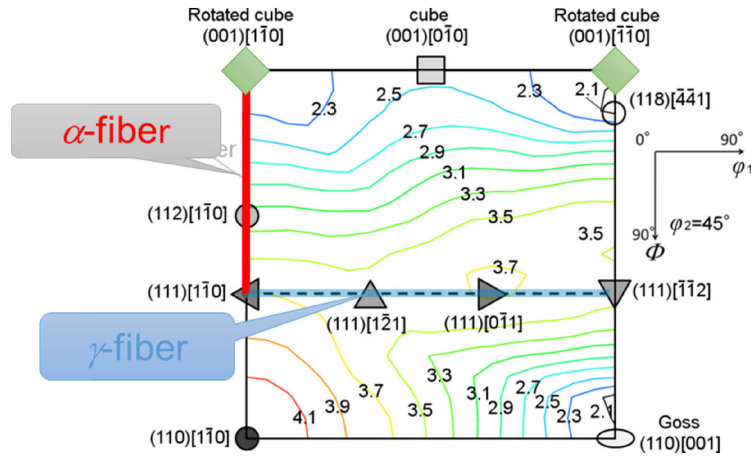
Fig. 11 $\varphi_2 = 45°$ section showing the Taylor factors for plane strain compression deformation of BCC materials. Slip systems $\{110\}\langle111\rangle$, $\{112\}\langle111\rangle$ and $\{123\}\langle111\rangle$ are taken into account.
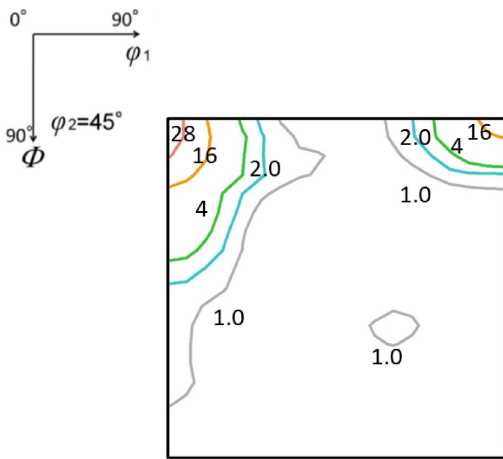

Fig. 12 $\varphi_2 = 45°$ section showing the orientation distribution after plane strain compression deformation of Fe–3.0 mass%Si at 1173 K with a strain rate of $5.0 \times 10^{-4}\,\text{s}^{-1}$ up to -1.0 in true strain. Formation of $\{001\}\langle110\rangle$ texture is confirmed, which corresponds with the prediction by the PDGG mechanism.
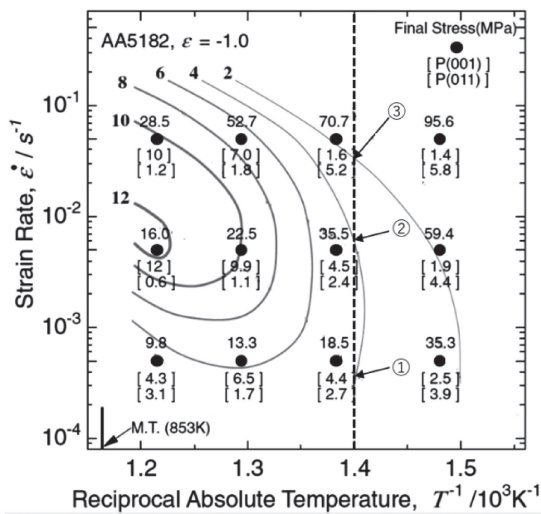

Fig. 13 The relationship between the pole density at [001], strain rate, and deformation temperature. The solid line curves show 2, 4, 6, 8, 10 and 12 times the mean pole density. Deformation conditions giving the development of [001] texture with 4 times and 2 times the mean pole density are marked by ① and ②, and ③ respectively.

commercial Al–Mg alloy AA5182 containing 4.5 mass%Mg after uniaxial compression deformation up to -1.0 in true strain. The maximum axis density at $\langle001\rangle$ is 12 times that of the random state in the range of deformation conditions shown here.

Figure 13 shows the important characteristics of the microstructure change accompanying the texture change during high temperature deformation: the texture development depends on both strain rate and temperature, and not on the function of flow stress. That is, the so-called Zener-Hollomon parameter is not useful in understanding this behavior. The same characteristics were also found in Fe–Si alloy.[6] Figure 13 indicates that the deformation at low temperature and high strain rate does not result in changes of microstructure and texture. Calvillo *et al.* have reported the same trend on Fe–2 mass%Si;[19] they carried out plane strain compression at 1173 K with a strain rate of $3.6\,\text{s}^{-1}$ and reported that the texture consisted of α and γ fiber with elongated grain structure in the mid-thickness layer.

The numerical values above the filled circles in Fig. 13 express the flow stress at a true strain of -1.0. The solid lines are contours corresponding to P(001) shown at the left end of each line. From this figure, strain rates giving P(001) = 4 and 2 at 713 K are determined as ① and ② for 4, and ③ for 2. The strain rates for ①, ② and ③ are determined as $4.0 \times 10^{-4}\,\text{s}^{-1}$, $5.0 \times 10^{-3}\,\text{s}^{-1}$, and $3.5 \times 10^{-2}\,\text{s}^{-1}$, respectively.

In Fig. 14, deformation conditions ①, ②, and ③ evaluated in Fig. 13 are plotted for a grain size of 100 μm in a high temperature deformation mechanism map reported for Al–5mol%(4.53 mass%)Mg alloy.[20] Figure 14 shows that the microstructure change accompanying the texture change occurs primarily in the region where solute atmosphere dragging of dislocations is the predominant mechanism of deformation. At the same time, this phenomenon is found to also occur where power law creep is the dominant mechanism of deformation, which suggests that the PDGG mechanism can operate when dislocations move under more or less the viscous effect of the solute atmosphere, even though the dominant rate controlling process is recovery.[13] That is, the PDGG mechanism might occurs to some extent whenever effective stress[14] exists.
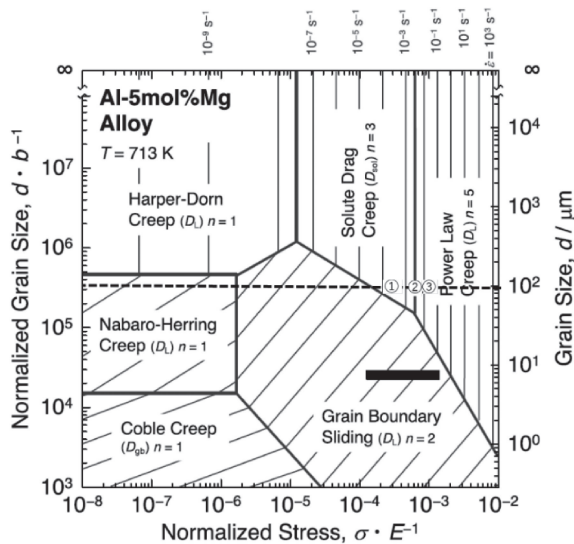
Fig. 14 Deformation conditions where the PDGG mechanism is active are plotted in the deformation mechanism map for Al–5mol%(4.53 mass%)Mg at 713 K as reported by Ito and Mizoguchi.[20]

6. Conclusions

The preferential dynamic grain growth (PDGG) mechanism, which was previously proposed to explain texture change accompanying microstructure change during high temperature deformation, was theoretically and experimentally investigated.

Because the PDGG mechanism can predict the texture on the basis of the orientation stability for deformation in a given deformation mode and the Taylor factor, experiments were conducted on solid solution alloys with FCC and BCC structures in two deformation modes: uniaxial compression and plane strain compression. Without exceptions, the experimental results were confirmed to correspond to the prediction.

It is shown that the Taylor factor reflects the dislocation density in the grains when the strain rate can be described by the following equation:

$$\dot{\varepsilon} = \beta \rho_{\mathrm{m}} \mathrm{bv} \tag{2}$$

A comparison of the experimental results investigating the conditions for the occurrence of the PDGG mechanism with the high temperature deformation mechanism map suggests that the PDGG mechanism works whenever effective stress exists. From this perspective, the PDGG mechanism is considered to occur in various materials and deformation conditions.

REFERENCES

1) K. Okayasu and H. Fukutomi: Proc. Int. Body Engineering Conference (IBEC2003), pp. 465–470.
2) S.R. Chen and U.F. Kocks: Texture and Microstructure Development in Al–2%Mg during High-Temperature Deformation. In: *Hot Deformation of Aluminum Alloys*, ed. by T.G. Langdon, H.D. Merchant, J.G. Morris and M.A. Zaidi, (TMS, Warrendale, 1991) pp. 89–104.
3) K. Okayasu, H. Takekoshi and H. Fukutomi: Mater. Trans. **48** (2007) 2002–2007.
4) K. Okayasu and H. Fukutomi: J. Japan Inst. Metals **70** (2006) 562–567.
5) K. Okayasu, H. Takekoshi, M. Sakakibara and H. Fukutomi: J. Japan Inst. Metals **73** (2009) 58–63.
6) Y. Onuki, R. Hongo, K. Okayasu and H. Fukutomi: Acta Mater. **61** (2013) 1294–1302.
7) H. Fukutomi and K. Okayasu: Proc. 8th Pacific Int. Congress on Advanced Materials and Processing (PRICM 8), ed. by FernD.S. Marquis, (Springer, 2016) pp. 965–972.
8) H. Fukutomi, S. Suzuki, I. Nakajima, K. Okayasu, M. Hasegawa and Y. Onuki: Tetsu-to-Hagané **107** (2021) 312–320.
9) M. Dahms and H.-J. Bunge: J. Appl. Crystallogr. **22** (1989) 439–447.
10) K. Pawlik: Phys. Status Solidi B **134** (1986) 477–483.
11) T.B. Massalski *et al.*: *Binary Alloy Phase Diagrams vol. 1*, (ASM, Ohio, 1986).
12) H.M. Jeong, K. Okayasu and H. Fukutomi: Mater. Trans. **51** (2010) 2162–2167.
13) H. Yoshinaga: J. JILM **39** (1989) 651–659.
14) H. Yoshinaga, K. Toma and S. Morozum: Trans. JIM **17** (1976) 559–570.
15) G.I. Taylor: J. Inst. Met. **62** (1938) 307–324.
16) G.Y. Chin and W.L. Mammel: Trans. TMS-AIME **239** (1967) 1400–1405.
17) Y. Onuki: Dr. Thesis, Yokohama National University https://ndlonline.ndl.go.jp/#!/detail/R300000001-I024821260-00
18) I.L. Dillamore, H. Katoh and K. Haslam: Texture **1** (1974) 151–156.
19) P. Rodriguez-Calvillo, Y. Houbaert, R. Petrov, L. Kesten and R. Colas: Mater. Chem. Phys. **136** (2012) 710–719.
20) T. Ito and T. Mizoguchi: Mater. Sci. Forum **941** (2018) 1216–1221.